



Testing and design of wire-laser additively manufactured high strength steel angle sections

Pengliang Yang¹, Yao Sun²

Abstract

Advanced additive manufacturing has revolutionized structural manufacturing by enabling previously impossible design freedom and precise material distribution control. This study focuses on the compressive capacity of high-strength steel angle section stub columns fabricated through the emerging wire-laser additive manufacturing technology. Fourteen angle section stub column specimens with varying leg widths and thicknesses were experimentally tested under axial compression. All tested specimens, regardless of their geometric dimensions, consistently failed by local buckling under compressive loading. Comparative analysis of experimental results and capacity predictions from the American and European codes revealed that the current specifications are conservative when applied to the design of WLAM high-strength steel plain angle sections under compression.

1. Introduction

In recent years, additive manufacturing (AM), commonly referred to as 3D-printing, has emerged as a transformative technology with significant potential to revolutionize the construction sector (Gardner 2023a). AM has gained widespread adoption across various industries, including aerospace (Blakey-Milner et al. 2021), biomedical (Kumar et al. 2021) and maritime (Vujović 2015) engineering. More recently, AM has been introduced in structural engineering, such as the world's first 3D-printed steel footbridge in Amsterdam (Gardner et al. 2020) and the 'Weave of Love' 3D-printed steel grid structure in Hong Kong (Panda3DP 2024). Compared to conventional manufacturing methods, AM provides several key benefits, including enhanced design flexibility, reduced material waste and lower equipment costs (Gardner 2023a; Sun 2025). These advantages make AM particularly well-suited for engineering applications involving structural high-strength steel (HSS), a high-performance construction material featuring high mechanical strength but often limited by high material costs (Sun et al. 2019; Zhao et al. 2023, 2024; Yang et al. 2025). By leveraging AM's precision and design adaptability, engineers can develop optimized structures that maximize material efficiency while minimizing waste. Consequently, AM presents a viable solution for expanding the use of HSS in structural applications.

Extensive research has been conducted on 3D-printed HSS components manufactured by wire-arc additive manufacturing (WAAM). WAAM builds up components by feeding wire feedstocks into

¹ Postdoctoral Research Fellow, College of Civil Engineering, Hunan University, <yangpengliang@hnu.edu.cn>

² Full Professor, College of Civil Engineering, Hunan University, <yaosun@hnu.edu.cn>

electric arc welding tools and selectively depositing the wires layer-by-layer (Kyvelou et al. 2020). Testing programs have been carried out on the material properties (Chen et al. 2025a; Chen and Sun 2025a; Huang et al. 2022; Rodrigues et al. 2020; Zhang et al. 2024), cross-sectional capacity (Weber et al. 2024) and member stability (Gardner et al. 2024; Weber et al. 2023) of WAAM HSS structures. Based on the test results, the existing design rules in ANSI/AISC 360 (AISC 2022) and EN 1993-1-12 (CEN 2025) were evaluated for their applicability to WAAM HSS structures. However, these studies also highlighted challenges when employing WAAM for HSS components, including inconsistency of material properties, uncertainty of structural response and undesirable geometric imperfections such as surface waviness, roughness and geometric distortion.

To overcome these shortcomings, wire-laser additive manufacturing (WLAM) has been recently developed (Yang and Sun 2026), which uses laser beams as the energy source and welding wires as the raw material. While both WAAM and WLAM employ wire melting during layer deposition, WLAM's laser energy source provides higher energy density (Roch et al. 2023) and reduced melt pool dimensions (Fotovvati et al. 2018), resulting in faster cooling rates and improved surface quality. Specifically, WLAM offers 0.7–3.5 kg/h deposition with an energy-specific rate around 0.87 kg/(h·kW), favoring thinner walls and precision features due to its lower heat input and better surface finish (Fotovvati et al. 2018; Roch et al. 2023). Additionally, WLAM enables finer microstructures, improving strength and fatigue resistance (Shim et al. 2025). The cost of producing HSS components using WLAM is comparable to WAAM in China, approximately 90 to 115 USD per kilogram (Rongsu Technology 2025). Existing research has predominantly focused on WLAM stainless steel. Goland et al. (2024) explored stress corrosion cracking behavior in nuclear environments. Bassis et al. (2022) examined corrosion performance through immersion tests and cyclic potentiodynamic polarization analysis. Chen and Sun (2025b) investigated the in-fire material response of WLAM austenitic stainless steel, and Sun and Chen (2025) also studied the local stability of WLAM stainless steel angle stub columns. However, no investigations have been conducted on the structural behavior of WLAM HSS components, which prompts the present study.

The present study focuses on the compression capacity of WLAM HSS equal-leg angle sections. HSS angle stub columns are used in practical applications such as lattice transmission towers, offshore platforms and bracing systems in high-rise buildings (Zhang et al. 2019). In these structures, angle members are often subjected to axial compression, and HSS allows for reduced material consumption while maintaining structural safety. This paper begins with the preparation of WLAM HSS angle specimens, followed by the testing program including fourteen stub column tests, geometric measurements and material testing using ER120S HSS. Finally, the suitability of design rules in ANSI/AISC 360-22 (AISC 2022) and EN 1993-1-12 (CEN 2025) for WLAM HSS angle sections is evaluated.

2. Additive manufacturing of test specimens

2.1. Manufacturing setup

A number of WLAM HSS equal-leg angle sections were manufactured using a Laser One 3D-printer (Rongsu Technology 2025) equipped with triple-vortex laser beam technology, as illustrated in Fig. 1. This technology employs three synchronized laser beams to achieve stable energy distribution, enhancing energy coupling efficiency and improving deposition quality.

ER120S HSS wires (1.2 mm diameter) were used as the deposition material. The angle sections were manufactured with layer orientations perpendicular to the longitudinal axis, with two nominal thicknesses of 3 mm and 5 mm to evaluate geometric scaling effects. The 3-mm-thick angles were manufactured using a single-pass strategy, while the 5-mm-thick angles adopted a zig-zag motion (Oluwadahunsi and Sun 2026). For single-pass printing, significant edge heat dissipation produces a parabolic weld profile, requiring a higher wire-feed ratio of 1.5 with a wire feeding rate of 7.5 mm/s and a travel speed of 5.0 mm/s to ensure sufficient cross-sectional filling. In contrast, the zig-zag approach achieves uniform filling through multi-pass overlapping with a pass width of 3.8 mm and spacing of 1.1 mm. The inter-pass overlap enables a dual fusion mechanism – heat accumulation enhances longitudinal fusion while overlap ensures transverse metallurgical bonding. As the zig-zag path covers a longer trajectory per layer, a lower wire-feed ratio of 1.0 with both speeds at 9.0 mm/s is sufficient. The manufacturing parameters align with those used in commercial production (Rongsu Technology 2025).

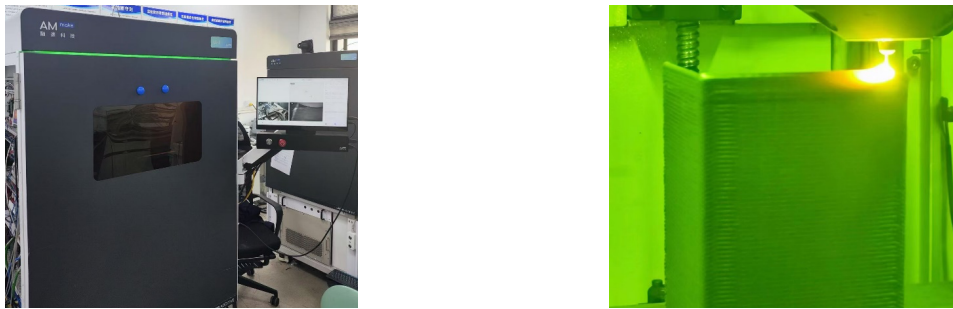
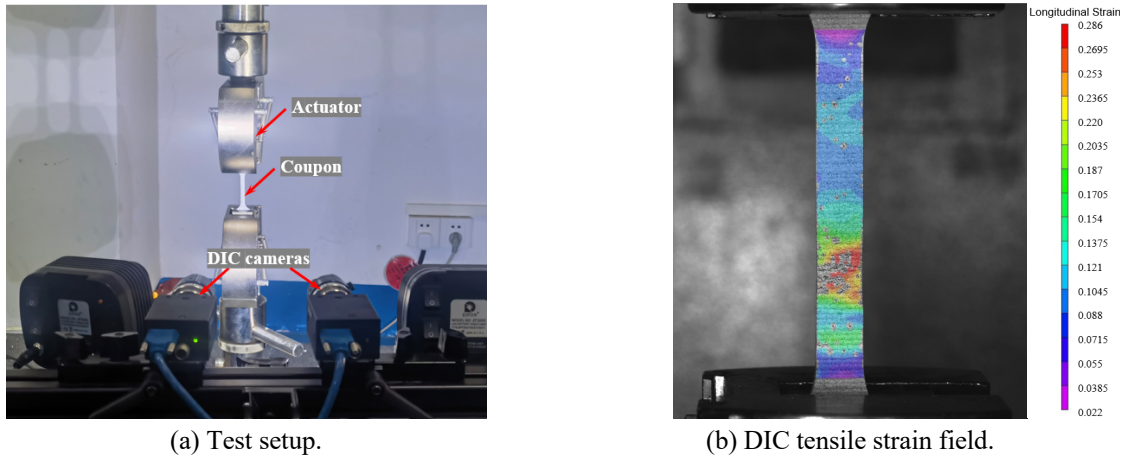


Figure 1: WLAM printing rig: (a) WLAM 3D-printer, (b) WLAM angle.



(a) Test setup.

(b) DIC tensile strain field.

Figure 2: Tensile coupon test.

2.2 Fabrication of WLAM stub columns and coupons

A total of fourteen WLAM HSS equal-leg angle stub columns were fabricated, comprising six leg widths (35 mm, 45 mm, 55 mm, 70 mm, 85 mm and 100 mm), and two leg thicknesses (3 mm and 5 mm). Two additional specimens – L-55×3 and L-70×5 – were fabricated for repeat tests. Each WLAM stub column specimen is labeled by its nominal leg width and thickness, with the suffix 'R' indicating a repeat specimen. The nominal column length was set as three times the leg width following Ziemian (2010), which is sufficiently long to contain representative imperfection patterns while preventing global buckling. The actual length L of each column was measured using

a measuring tape. Additionally, two longitudinal coupons were extracted from each material thickness using wire-cutting electrical discharge machining, with dimensions following GB/T 228-1 (2021).

3. Testing program

3.1. Material testing

Material tests were conducted to determine the properties of WLAM ER120S HSS. All four coupons were tested under tensile loading in a 100 kN testing machine following GB/T 228-1 (2021), as shown in Fig. 2(a). A displacement-controlled loading scheme was adopted, with an initial loading rate of 0.05 mm/min increasing to 0.4 mm/min after reaching the nominal yield strength (Huang and Young 2014). A digital image correlation (DIC) system was employed to capture strain distributions, with a representative strain field shown in Fig. 2(b), indicating strain concentration in the central region leading to fracture.

The measured stress-strain curves are presented in Fig. 3, with key material properties summarized in Table 1, including Young’s modulus E , yield strength f_y , ultimate strength f_u , fracture strain ϵ_f and ultimate-to-yield strength ratio f_u / f_y . The two pairs of coupons exhibit similar stress-strain responses, indicating negligible difference between the two material thicknesses. Compared to conventionally manufactured HSS that exhibits an obvious yield plateau, the WLAM ER120S HSS displays a more rounded stress-strain response with significant strain hardening, as reflected by the high f_u / f_y ratios in Table 1. This may be attributed to the cyclic thermal history during layer-by-layer deposition, which promotes grain refinement and localized strengthening mechanisms. Similar trends have been reported in other additively manufactured steels (Nie et al. 2016; Zhu et al. 2022).

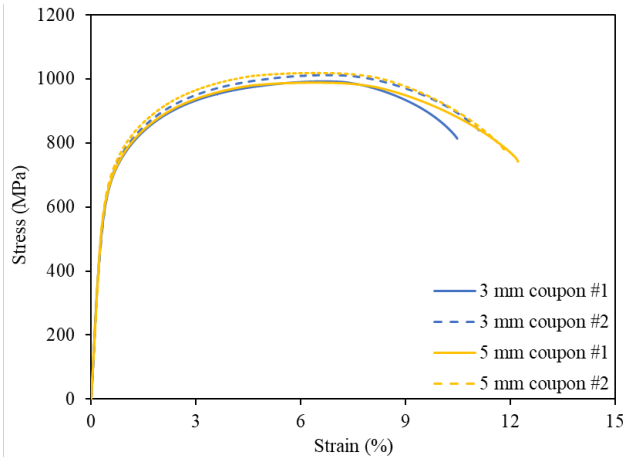


Figure 3: Measured stress–strain curves.

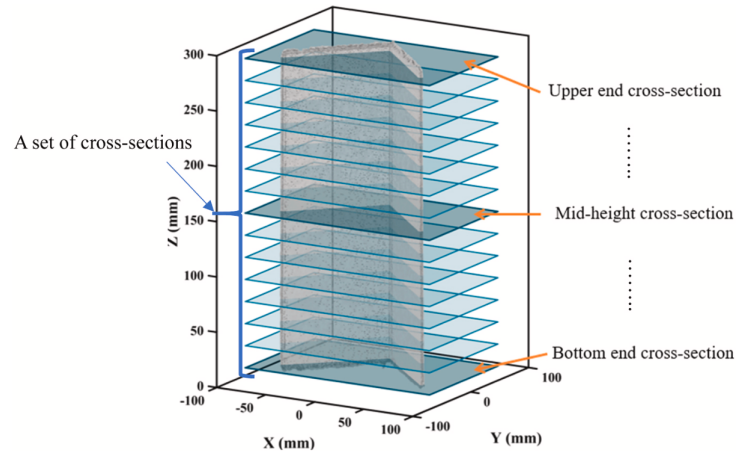


Figure 4: Selection of a set of cross-sections for geometric analysis.

Table 1: Measured material properties of WLAM ER120S HSS.

Material thickness	Coupon	E (GPa)	f_y (MPa)	f_u (MPa)	ϵ_f (%)	f_u / f_y
3 mm	Coupon #1	203.7	664.3	992.5	12.4	1.49
	Coupon #2	205.2	667.2	1012.0	13.6	1.52
5 mm	Coupon #1	204.6	665.2	988.7	12.9	1.49
	Coupon #2	206.4	667.4	1018.7	14.1	1.53

3.2. Measurements of geometric properties

Prior to stub column tests, the geometric properties of WLAM HSS specimens were quantified using 3D laser scanning. Full-surface point cloud data were captured and reconstructed into models via Rhinoceros 3D software and processed in MATLAB. The raw data were filtered to eliminate noise and aligned using Principal Component Analysis (PCA) to ensure cross-sections were extracted perpendicular to the specimen length. A set of uniformly distributed cross-sections were then selected along the column length, as illustrated in Fig. 4 for specimens L-100×3. A sensitivity study on cross-section spacing ($L/100$, $L/50$, $L/30$ and $L/7$) indicated that $L/30$ provides the optimal balance between accuracy and efficiency and was adopted for all fourteen specimens.

The leg width b was taken as the average value from the selected cross-sections, as shown in Fig. 5 for specimen L-100×3. The differences between actual and nominal leg widths lie within ± 2 mm, which is smaller than the dimensional variation of WAAM (± 5 mm) but less accurate than selective laser melting (± 1 mm). The centerlines of the selected cross-sections were generated by linear regression of the measured point clouds in MATLAB. For each cross-section, the leg thickness t is defined as twice the average distance from data points to the fitted centerlines (Chen et al. 2025b). The local imperfections (ω_i) were calculated as deviations from data points to the fitted centerlines minus half the leg thickness, with the maximum value taken as the local imperfection amplitude (ω_l) (see Table 2). Surface roughness parameters were calculated following ISO 25178-2 (ISO 2021), where S_a is the arithmetical mean height, S_q is the root mean square height, S_k is the surface skewness, and S_{ku} is the surface kurtosis. The S_a values range from 0.05 mm to 0.13 mm, significantly lower than WAAM components (0.18–0.40 mm) (Evans et al. 2023; Evans et al. 2024), indicating smoother surface finishes produced by the WLAM process.

Table 2: Measured geometries of WLAM angle stub columns.

Specimen	L (mm)	b (mm)	t (mm)	ω_l (mm)	S_a (um)	S_q (um)	S_k	S_{ku}	ϕ_{\max} (°)
L-35×3	104.6	35.3	3.06	0.14	0.07	0.10	0.84	1.86	-0.21
L-45×3	135.5	45.7	3.04	0.17	0.05	0.09	0.79	1.93	0.33
L-55×3	163.6	53.8	3.04	0.16	0.07	0.08	0.90	1.84	0.28
L-55×3-R	164.3	54.8	2.99	0.20	0.11	0.13	1.01	1.91	0.31
L-70×3	210.6	71.7	2.98	0.13	0.08	0.10	0.93	1.87	-0.27
L-85×3	254.1	86.4	3.03	0.20	0.12	0.14	0.96	1.81	-0.18
L-100×3	300.5	101.9	3.10	0.19	0.11	0.13	0.88	1.94	-0.26
L-35×5	105.3	35.5	4.85	0.13	0.05	0.09	0.73	1.88	-0.18
L-45×5	135.4	45.4	4.97	0.14	0.07	0.11	0.85	1.90	0.21
L-55×5	165.1	54.1	4.93	0.15	0.07	0.09	0.92	1.83	0.23
L-70×5	209.1	70.8	4.97	0.17	0.09	0.13	0.84	1.92	0.27
L-70×5-R	209.3	71.3	4.95	0.17	0.13	0.15	0.93	1.86	-0.25
L-85×5	253.5	84.3	4.96	0.19	0.11	0.15	0.81	1.95	-0.24
L-100×5	299.2	102.1	4.88	0.22	0.07	0.10	0.84	1.86	-0.21

Finally, the leg thickness of each WLAM angle specimen was taken as the average of the derived values from the selected cross-sections, while the local imperfection amplitude (ω_l) was taken as the maximum deviation, as summarized in Table 2. Based on the determined leg width and

thickness, a constant cross-section model was developed for each stub column and overlapped with the scanned model to illustrate geometric undulations from the WLAM process, as illustrated in Fig. 6 for specimen L-100×3. The initial twist imperfections φ were also determined along the member length, following procedures in Evans et al. (2023). The maximum twist imperfection amplitudes φ_{max} for the fourteen stub column specimens are reported in Table 2.

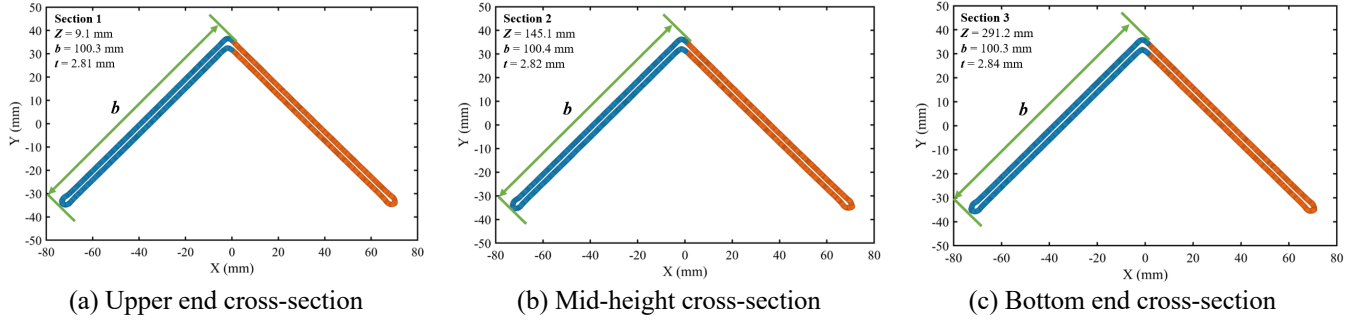


Figure 5: Geometric analysis of selected typical cross-sections.

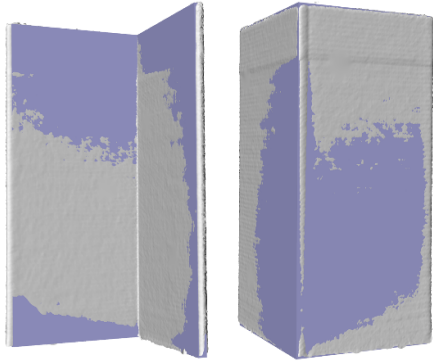


Figure 6: Illustration of geometric undulations.

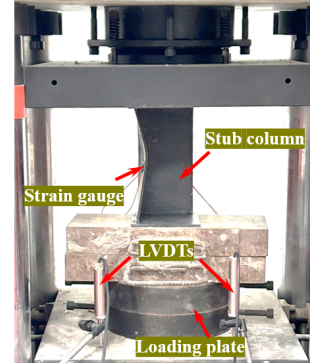


Figure 7: Stub column test rig.

3.3. Stub column compressive tests

The fourteen WLAM HSS equal-leg angle stub columns were tested under axial compressive loading to investigate their cross-sectional capacity. Before testing, each stub column was milled to achieve flat and parallel ends, and two 6-mm-thick end plates were welded to ensure uniform stress distribution. The test apparatus, as shown in Fig. 7, comprised two strain gauges affixed to the angle legs at mid-height for measuring axial strains, and two LVDTs positioned at both ends for monitoring specimen end-shortenings. The specimens were compressed concentrically at a loading rate of 0.2 mm/min (Sun et al. 2024a; Sun et al. 2024b). All measured data, including compression loads, end-shortenings and longitudinal strains, were recorded using a DATASCAN data acquisition system.

The failure modes of typical WLAM HSS equal-leg angle stub columns are shown in Fig. 8, featuring pronounced localized deformations at mid-height, indicative of local buckling failure. The load-end shortening curves are plotted in Fig. 9, with main test results reported in Table 3, including ultimate loads N_u and the corresponding end-shortenings δ_u , and the ultimate-to-yield load ratios $N_u / (Af_y)$. The specimens exhibit constant stiffness in the initial elastic stage, primarily dependent on geometric dimensions and material Young's modulus. As the applied load increases, the slopes of the curves decrease, indicating stiffness reduction and onset of localized deformations.

As shown in Fig. 9 and Table 3, the WLAM HSS angle stub columns generally exhibit higher compressive capacities as cross-sectional dimensions increase. The repeat specimens (L-55×3/L-55×3-R and L-70×5/L-70×5-R) display very similar load-carrying capacities and load-deformation responses, demonstrating the reliability of the stub column tests and WLAM technology. However, the ultimate-to-yield load ratios $N_u / (Af_y)$ gradually decrease with increasing width-to-thickness ratios b / t , as shown in Fig. 10. For specimens with the same leg thickness, there is no significant change in load-carrying capacity for very slender sections with large b / t ratios. For instance, the capacities of L-70×3, L-85×3 and L-100×3 are 182.0 kN, 185.9 kN and 187.6 kN respectively, showing only minor variations. This suggests that once the angle section reaches a certain slenderness limit, further increases in b / t ratio do not significantly impact its load-carrying capacity, as the failure becomes governed by local buckling rather than material yielding.

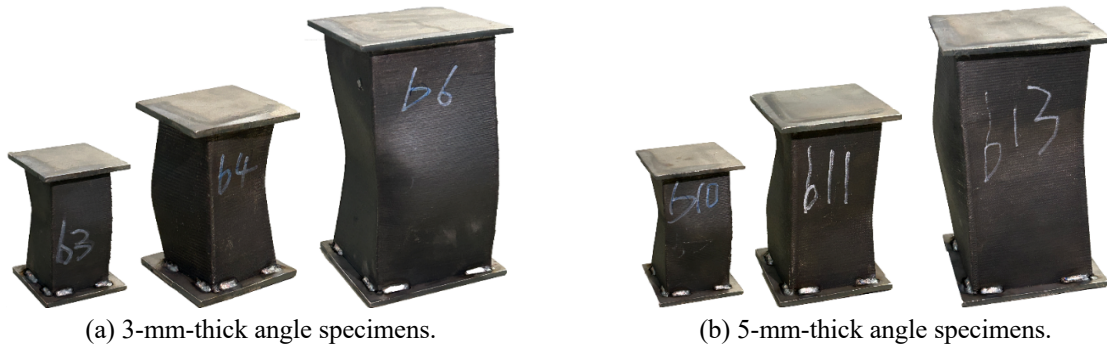
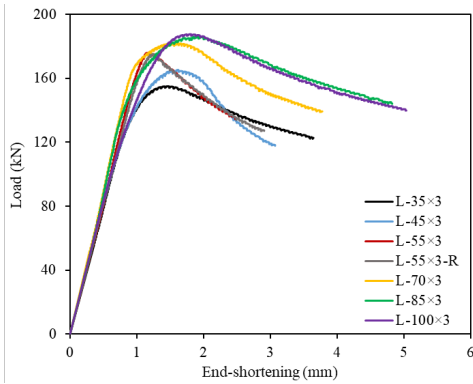
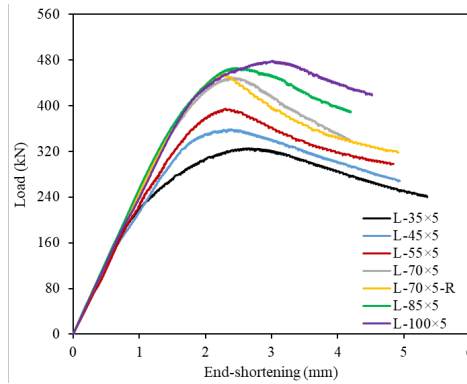


Figure 8: Failure mode of representative WLAM HSS angles.



(a) 3-mm-thick angle specimens.



(b) 5-mm-thick angle specimens.

Figure 9: Measured load–deformation curves.

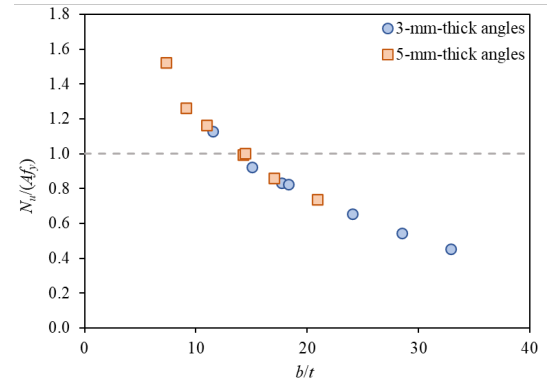


Figure 10: Ultimate-to-yield load ratios of WLAM HSS angle stub columns.

Table 3: Key stub column test results.

Specimen	N_u (kN)	δ_u (mm)	$N_u / (Af_y)$	Specimen	N_u (kN)	δ_u (mm)	$N_u / (Af_y)$
L-35×3	155.1	1.43	1.13	L-35×5	325.3	2.62	1.52
L-45×3	165.2	1.61	0.92	L-45×5	358.8	2.33	1.26
L-55×3	175.9	1.15	0.83	L-55×5	394.5	2.39	1.16
L-55×3-R	175.3	1.27	0.83	L-70×5	449.9	2.49	0.99
L-70×3	182.0	1.50	0.65	L-70×5-R	454.8	2.40	1.00
L-85×3	185.9	1.73	0.54	L-85×5	466.1	2.42	0.86
L-100×3	187.6	1.74	0.45	L-100×5	478.8	3.02	0.74

4. Design analysis

4.1. General

Upon completing the laboratory experiments, a design analysis is presented herein. The design guidelines codified in ANSI/AISC 360-22 (AISC 2022) and EN 1993-1-12 (CEN 2025) for conventionally manufactured HSS structures were described, and their suitability for WLAM HSS stub columns was assessed based on the test results. The quantitative evaluations for both design methods are summarized in Table 4, including the mean test-to-predicted capacity ratios ($N_u / N_{u,pred}$). To facilitate comparison, Figs. 11-14 illustrate graphical comparisons between experimental capacities and predicted values for detailed assessment.

Table 4: Assessment of design methods for WLAM HSS angles.

Cross-section	ANSI/AISC 360-22 [21] mean $N_u / N_{u,AISC}$	EN 1993-1-12 [22] mean $N_u / N_{u,EC3}$
Nonslender angles	1.464	1.475
Slender angles	1.497	1.552
Overall	1.483	1.519

4.2. American specification ANSI/AISC 360-22

Since stub columns are sufficiently short to prevent global buckling, their compressive capacities are governed by cross-sectional behavior. ANSI/AISC 360-22 (AISC 2022) is an American design specification for steel structures with grades up to S690. Regarding cross-sections in compression, ANSI/AISC 360-22 (AISC 2022) uses a classification framework that classifies cross-sections as slender and nonslender sections. Nonslender sections are capable of achieving cross-sectional yield loads Af_y , whilst their slender counterparts fail prior to the attainment of Af_y owing to the occurrence of elastic local instability. For an equal-leg angle subjected to compression, the classification is determined by comparing its width-to-thickness ratio b / t against the limiting ratio of $0.45(E / f_y)^{0.5}$. The limiting ratio is graphically assessed in Fig. 11 based upon the test data normalized by the cross-sectional yield loads Af_y , showing that the existing limiting ratio cannot accurately represent the boundary between slender angles (i.e. those with $N_u / (Af_y) < 1$) and nonslender angles (i.e. those with $N_u / (Af_y) > 1$) in Fig. 11. Regarding the design compressive capacity of equal-leg angles, ANSI/AISC 360-22 (AISC 2022) specifies the yield load Af_y for nonslender angles and the effective load $A_{eff,AISC}f_y$ for slender angles, where $A_{eff,AISC}$ is the AISC effective sectional area determined from the effective width method to account for elastic local instability. The effective leg width is calculated as the original leg width multiplied by the reduction factor ρ_{AISC} given in Eq. (1), where f_{el} denotes the sectional elastic local buckling stress, derived from Eq. (2).

$$\rho_{AISC} = \left(1 - 0.22 \sqrt{\frac{f_{el}}{f_y}} \right) \sqrt{\frac{f_{el}}{f_y}} \quad (1)$$

$$f_{el} = \frac{0.45E}{(b/t)^2} \quad (2)$$

The applicability of ANSI/AISC 360-22 (AISC 2022) to WLAM HSS equal-leg angle sections is examined based on test results. The experimental ultimate loads normalized by predicted capacities ($N_u / N_{u,AISC}$) are plotted against b / t ratios in Fig. 12, showing similar design accuracy for both 3-mm-thick and 5-mm-thick specimens. The mean capacity ratios $N_u / N_{u,AISC}$ are 1.464 and 1.497 for nonslender and slender angles respectively, as summarized in Table 4. Both Fig. 12 and Table

4 reveal under-estimation of capacities for WLAM HSS angle sections. The conservatism for nonslender angles is mainly due to the neglect of significant material strain hardening, while for slender angles it is attributed to the inaccurate nature of the AISC effective width method. The WLAM HSS angles are also compared with conventionally manufactured (CM) HSS angles from previous studies in Fig. 12. The AISC method also yields conservative predictions for conventional HSS angles with mean $N_u / N_{u,AISC}$ of 1.395, but shows slightly lower accuracy for WLAM HSS angles due to their higher degree of material strain hardening.

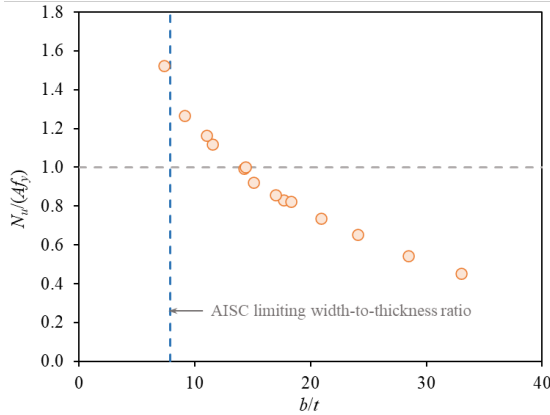


Figure 11: Assessment of AISC limiting width-to-thickness ratio.

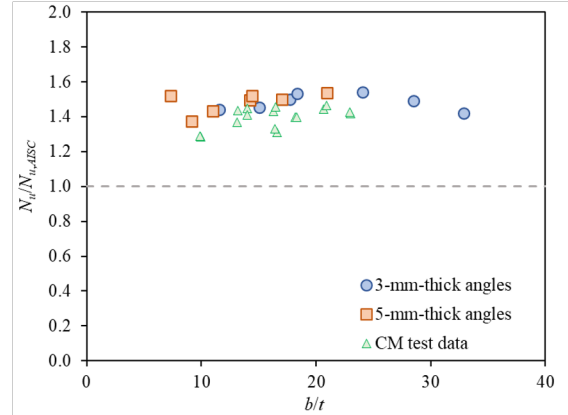


Figure 12: Evaluation of AISC design capacities.

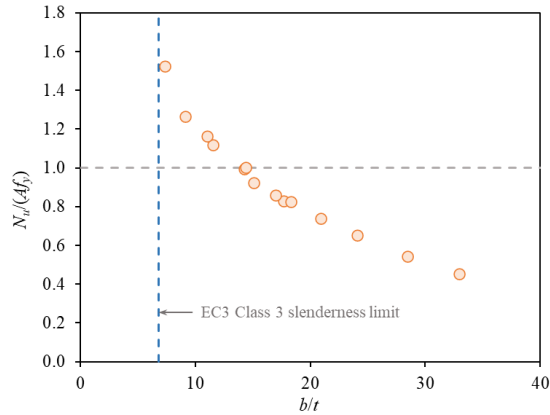


Figure 13: Assessment of EC3 slenderness limit.

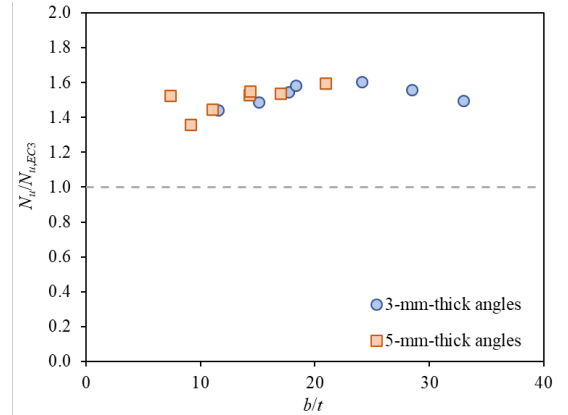


Figure 14: Evaluation of EC3 design capacities.

4.3. Eurocode EN 1993-1-12

As part of the latest version of Eurocode 3, EN 1993-1-12 (CEN 2025) provides design guidelines for HSS structures with grades up to S960. Similar to its American counterpart (AISC 2022), EN 1993-1-12 (CEN 2025) also adopts cross-section classification, categorizing sections in compression as nonslender (Class 1-3) and slender (Class 4) sections. The classification is performed by comparing the leg width-to-thickness ratio b / t against the Class 3 slenderness limit of 11.5ε , where $\varepsilon = (235/f_y)^{0.5}$ is the material parameter. Once the section classification is completed, EN 1993-1-12 (CEN 2025) specifies the yield load $A f_y$ for nonslender angles and effective load $A_{eff,EC3} f_y$ for slender angles as the design compressive capacity $N_{u,EC3}$. The EC3 effective sectional area $A_{eff,EC3}$ is determined using the effective width concept, with a reduction factor ρ_{EC3} defined in Eq. (3), where λ_p is the plate slenderness, as calculated from Eq. (4).

$$\rho_{EC3} = \frac{\lambda_p - 0.188}{\lambda_p^2} \leq 1 \quad (3)$$

$$\lambda_p = \frac{b/t}{18.6\varepsilon} \quad (4)$$

The EC3 provisions are assessed qualitatively and quantitatively based on experimental data. The test failure loads normalized by the sectional yield loads are plotted in Fig. 13 to assess the suitability of the EC3 Class 3 slenderness limit of 11.5ε for WLAM HSS angles, showing similar inaccuracy as observed for the AISC limit. The ultimate load ratios $N_u / N_{u,EC3}$ are presented in Fig. 14 and Table 4. Both graphical and quantitative results indicate that EC3 provisions lead to conservative predictions for angle sections. The conservatism for nonslender angles is mainly due to the neglect of material strain hardening, from which nonslender angles can benefit for their capacities. For slender angles, the conservatism is attributed to the conservative nature of the EC3 effective width method. Overall, EN 1993-1-12 (CEN 2025) (mean $N_u / N_{u,EC3} = 1.519$) is more conservative than ANSI/AISC 360-22 (AISC 2022) (mean $N_u / N_{u,AISC} = 1.483$).

5. Conclusions

The compression capacity of WLAM HSS equal-leg angles has been systematically investigated through laboratory experiments and design analyses. Fourteen stub column specimens with six leg widths (35–100 mm) and two thicknesses (3 mm and 5 mm) were tested under axial compression, alongside tensile coupon tests and 3D-scanning for geometric measurements. All specimens exhibited localized deformation failure, with the ultimate-to-yield load ratio showing an inverse correlation to width-to-thickness ratio. Two design approaches – ANSI/AISC 360-22 and EN 1993-1-12 – were evaluated for their applicability to WLAM HSS angles. Both codes result in conservative predictions, with mean actual-to-predicted compressive capacity values of 1.483 and 1.519 for AISC and EC3 respectively. The conservatism for nonslender angles is attributed to strain hardening effects not considered in the codes, while for slender angles the under-prediction is due to the conservative effective width methodology.

Acknowledgments

This work is jointly supported by the grant from the Natural Science Foundation of Hunan Province of China (No.: 2025JJ60293) and the Fundamental Research Funds for the Central Universities (No: 020100-531119200260).

References

- AISC (American Institute of Steel Construction). (2022). “Specification for structural steel buildings.” ANSI/AISC 360-22, The United States.
- Bassis, M., Ron, T., Leon, A., Kotliar, A., Kotliar, R., Shirizly, A., Aghion, E. (2022). “The Influence of intralayer porosity and phase transition on corrosion fatigue of additively manufactured 316L stainless steel obtained by direct energy deposition process.” *Materials*, MDPI, 15 (16) 5481.
- Blakey-Milner, B., Gradl, P., Snedden, G., Brooks, M., Pitot, J., Lopez, E., Leary, M., Berto, F., Du Plessis, A. (2021). “Metal additive manufacturing in aerospace: A review.” *Materials & Design*, Elsevier, 209, 110008.
- CEN (European Committee for Standardization). (2025). “Design of steel structures – Part 1.12: Additional rules for the extension of EN 1993 up to steel grades S700.” Eurocode 3, prEN 1993-1-12:2025, Brussels, Belgium.
- Chen, W., Wang, Z., Xuan, Y., Guo, S., Zhou, Q., Peng, Y., Wang, K. (2025a). “Investigation on deformation behavior of high strength laminated heterostructured materials of ER120S-G high strength steel and 316L stainless steel fabricated by Wire-arc DED.” *Materials Science and Engineering: A*, Elsevier, 923, 147750.
- Chen, X., Zhao, O., Xu, F., Zhi, J., Sun, Y. (2025b). “Cross-sectional capacity of wire arc additively manufactured stainless steel channel section stub columns.” *Journal of Structural Engineering*, ASCE, 151 (6) 04025057.

- Chen, X., Sun, Y. (2025a). “Experimental investigation of mechanical properties of 3D-printed normal-strength and high-strength steels.” *Journal of Constructional Steel Research*, Elsevier, 234, 109773.
- Chen, X., Sun, Y. (2025b). “In-fire behavior of wire-laser additively manufactured austenitic stainless steel.” *Construction and Building Materials*, Elsevier, 493, 143304.
- Evans, S.I., Hadjipantelis, N., Wang, J. (2024). “Stub column tests on wire arc additively manufactured equal-leg angle sections.” *Engineering Structures*, Elsevier, 317, 118591.
- Evans, S.I., Xu, F., Wang, J. (2023). “Material properties and local stability of WAAM stainless steel equal angle sections.” *Engineering Structures*, Elsevier, 287, 116160.
- Fotovvati, B., Wayne, S.F., Lewis, G., Asadi, E. (2018). “A Review on Melt - Pool Characteristics in Laser Welding of Metals.” *Advances in Materials Science and Engineering*, Wiley, 2018 (1) 4920718.
- Gardner, L. (2023a). “Metal additive manufacturing in structural engineering—review, advances, opportunities and outlook.” *Structures*, Elsevier, 47, 2178-2193.
- Gardner, L., Kyvelou, P., Herbert, G., Buchanan, C. (2020). “Testing and initial verification of the world's first metal 3D printed bridge.” *Journal of Constructional Steel Research*, Elsevier, 172, 106233.
- Gardner, L., Li, J., Meng, X., Huang, C., Kyvelou, P. (2024). “I-section steel columns strengthened by wire arc additive manufacturing—concept and experiments.” *Engineering Structures*, Elsevier, 306, 117763.
- GB/T 228-1:2021. (2021). “Metallic materials—Tensile testing—Part 1: Method of test at room temperature.” Standardization Administration of China.
- Goland, M., Balbaud, F., Fouchereau, A., Guerre, C., Nguejio, J., Puga, B., Rousseau, M., Cailloux, T., Maskrot, H., Pacquentin, W. (2024). “Corrosion behavior of additively manufactured stainless steels in nuclear environments.” *Advances in Materials Technology for Power Plants*, 84871, 23-38.
- Huang, C., Kyvelou, P., Zhang, R., Britton, T.B., Gardner, L. (2022). “Mechanical testing and microstructural analysis of wire arc additively manufactured steels.” *Materials & Design*, Elsevier, 216, 110544.
- Huang, Y., Young, B. (2014). “The art of coupon tests.” *Journal of Constructional Steel Research*, Elsevier, 96, 159-175.
- ISO (International Organization for Standardization). (2021). “Geometrical product specifications (GPS) — Surface texture: Areal — Part 2: Terms, definitions and surface texture parameters. ISO 25178-2:2021.” Switzerland.
- Kumar, R., Kumar, M., Chohan, J.S. (2021). “The role of additive manufacturing for biomedical applications: A critical review.” *Journal of Manufacturing Processes*, Elsevier, 64, 828-850.
- Kyvelou, P., Slack, H., Mountanou, D.D., Wade, M.A., Britton, T.B., Buchanan, C., Gardner, L. (2020). “Mechanical and microstructural testing of wire and arc additively manufactured sheet material.” *Materials & Design*, Elsevier, 192, 108675.
- Nie, Z., Wang, G., McGuffin-Cawley, J.D., Narayanan, B., Zhang, S., Schwam, D., Rong, Y.K. (2016). “Experimental study and modeling of H13 steel deposition using laser hot-wire additive manufacturing.” *Journal of Materials Processing Technology*, Elsevier, 235, 171-186.
- Oluwadahunsi, S. E., Sun, Y. (2026). “Testing and design of stainless steel channel stub columns 3d-printed by wire-laser additive manufacturing.” *Journal of Structural Engineering*, 152(2), 04025268.
- Panda3DP (2024). “A grand 5.3-meter metal 3D-printed sculpture debuts in Hong Kong: WAAM technology by AMmake revolutionizes complex architectural creations.” <https://panda3dp.com/3dprintnews-6223-1.html> (accessed 07 September 2025).
- Roch, C., Tournier, C., Lavernhe, S. (2023). “Process based modelling of power density for wire laser additive manufacturing using a coaxial head.” *Additive Manufacturing*, Elsevier, 73, 103648.
- Rodrigues, T.A., Duarte, V.R., Tomás, D., Avila, J.A., Escobar, J.D., Rossinyol, E., Oliveira, J.P. (2020). “In-situ strengthening of a high strength low alloy steel during Wire and Arc Additive Manufacturing (WAAM).” *Additive Manufacturing*, Elsevier, 34, 101200.
- Rongsu Technology. (2025). “AMmake R1 series for 3D printing.” <https://www.rongsu.com/#/production/r1> (accessed 07 September 2025).
- Shim, Y.R., Kim, J.K., Jo, D.H., Yang, H.P., Yoon, S.W., Yu, U.Y., Jeon, J.B. (2025). “Microstructure and Mechanical Properties of Wire Laser Additive Manufactured Deposits and Their Tungsten Inert Gas Welds.” *Materials*, MDPI, 18 (6) 1308.
- Sun, Y., Liang, Y., Zhao, O. (2019). “Testing, numerical modelling and design of S690 high strength steel welded I-section stub columns.” *Journal of Constructional Steel Research*, Elsevier, 159, 521-533.
- Sun, Y. (2025). “In-fire material properties of wire-arc additively manufactured 3D-printed structural aluminum alloys.” *Construction and Building Materials*, Elsevier, 474, 140946.
- Sun, Y., Chen, X. (2025). “Testing and design of wire-laser additively manufactured (WLAM) stainless steel angle section stub columns.” *Thin-Walled Structures*, Elsevier, 113351.

- Sun, Y., Wang, Z., Xia, J., Chen, X. (2024a). "Tests, simulations and design of aluminium alloy equal-leg angle section stub columns after exposure to fire." *Engineering Structures*, Elsevier, 314, 118405.
- Sun, Y., Wang, Z., Xia, J., Sarquis, F.R., de Lima, L.R. (2024b). "Experimental and numerical study of aluminium alloy angle-section stub columns." *Thin-Walled Structures*, Elsevier, 205, 112361.
- Vujović, I. (2015). "The introduction of 3D printing into the Maritime Industry." *Transactions on Maritime Science*, 4 (01) 86-87.
- Weber, B., Meng, X., Nitawaki, M., Gardner, L. (2023). "Optimisation and testing of simply - supported WAAM beams." *ce/papers*, 6 (3-4) 708-713.
- Weber, B., Meng, X., Zhang, R., Nitawaki, M., Sagawa, T., Gardner, L. (2024). "Tensile behaviour of WAAM high strength steel material and members." *Materials & Design*, Elsevier, 237, 112517.
- Yang, P., Sun, Y. (2026). "Cross-sectional capacity of wire-laser additively manufactured (WLAM) high-strength steel angle stub columns." *Engineering Structures*, Elsevier, 348, 121748.
- Yang, P., Chen, C., & Sun, Y. (2025). "Machine learning-based design for high-strength steel tubular section columns." *Structures*, Elsevier, 80, 109872.
- Zhang, J., Fan, J., Duan, L., Chen, W., Yang, D., Wang, K. (2024). "The mechanical properties and microstructural evolution of 14Ni3Cr3Mo1MnTiAl high strength steel fabricated by WAAM." *Materials Science and Engineering: A*, Elsevier, 901, 146565.
- Zhao, J., Li, J., Sun, Y. (2023). "Experimental and numerical study on overall buckling behavior of Q460 high-strength steel continuous beams with welded singly symmetric I-section." *Engineering Structures*, Elsevier, 280, 115678.
- Zhao, J., Li, J., McDermott, P., Wang, J., Chen, X., Sun, Y. (2024). "Global stability of mono-symmetric I-section high-strength steel beams." *Structures*, Elsevier, 68, 107230.
- Zhu, L., Geng, K., Wang, J., Sun, D., Shan, M., Lu, Y., Jiang, Z. (2022). "Strain hardening and strengthening mechanism of laser melting deposition (LMD) additively manufactured FeCoCrNiAl0.5 high-entropy alloy." *Materials Characterization*, Elsevier, 194, 112365.
- Ziemian, R.D. (2010). "Guide to stability design criteria for metal structures." John Wiley & Sons.